# Manipulating Migration Behavior of Magnetic Graphene Oxide via Magnetic Field Induced Casting and Phase Separation toward High-Performance Hybrid Ultrafiltration Membranes

Zhiwei Xu,* Tengfei Wu, Jie Shi, Wei Wang, Kunyue Teng, Xiaoming Qian,* Mingjing Shan, Hui Deng, Xu Tian, Cuiyu Li, and Fengyan Li

State Key Laboratory of Separation Membranes and Membrane Processes, School of Textiles, Tianjin Polytechnic University, Tianjin 300387, China

Ⓢ Supporting Information
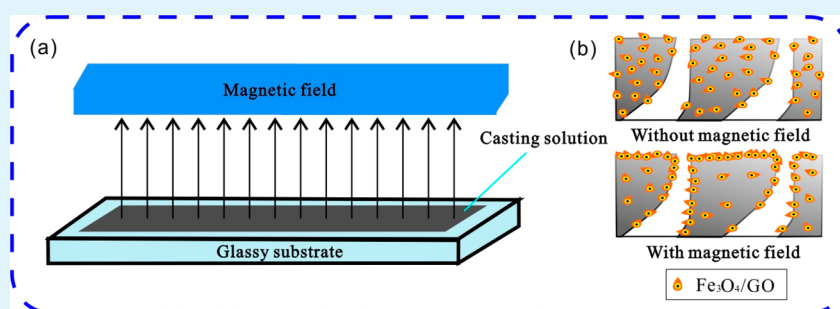
ABSTRACT: Hybrid membranes blended with nanomaterials such as graphene oxide (GO) have great opportunities in water applications due to their multiple functionalities, but they suffer from low modification efficiency of nanomaterials due to the fact that plenty of the nanomaterials are embedded within the polymer matrix during the blending process. Herein, a novel Fe_3O_4/GO−poly(vinylidene fluoride) (Fe_3O_4/GO−PVDF) hybrid ultrafiltration membrane was developed via the combination of magnetic field induced casting and a phase inversion technique, during which the Fe_3O_4/GO nanocomposites could migrate toward the membrane top surface due to magnetic attraction and thereby render the surface highly hydrophilic with robust resistance to fouling. The blended Fe_3O_4/GO nanocomposites migrated to the membrane surface with the magnetic field induced casting, as verified by X-ray photoelectron spectroscopy, elemental analysis, and energy dispersive X-ray spectroscopy. As a result, the novel membranes exhibited significantly improved hydrophilicity (with a contact angle of 55.0°) and water flux (up to 595.39 L m^{-2} h^{-1}), which were improved by 26% and 206%, 12% and 49%, 25% and 154%, and 11% and 33% compared with those of pristine PVDF membranes and PVDF hybrid membranes blended with GO, Fe_3O_4, and Fe_3O_4/GO without the assistance of magnetic field during membrane casting, respectively. Besides, the novel membranes showed high rejection of bovine serum albumin (>92%) and high flux recovery ratio (up to 86.4%). Therefore, this study presents a novel strategy for developing high-performance hybrid membranes via manipulating the migration of nanomaterials to the membrane surface rather than embedding them in the membrane matrix.

KEYWORDS: graphene oxide, Fe_3O_4, hybrid membrane, magnetic field, migration behavior

1. INTRODUCTION

Membrane technology has advanced significantly in the past few decades for water purification and wastewater treatment, among which polymeric membranes have evolved as one of the most promising alternatives by virtue of their low cost, good processability, high flexibility, etc.[1,2] Nevertheless, the inherent hydrophobicity of commercially used polymeric membranes [e.g., polyvinylidene fluoride (PVDF), polypropylene and poly(ether sulfone)] induces a high tendency toward membrane fouling, which can diminish the separation performance and shorten membrane life, thereby restricting the advancements of membrane technology.[3,4] To date, hydrophilicity modification of polymeric membranes is the primary approach for mitigating membrane fouling.[5,6]

Generally, hydrophilic modification of polymeric membranes primarily consisted of surface modification and blending modification.[7,8] Ongoing development of surface modification has enabled the integration of hydrophilic or superhydrophilic materials on a membrane surface by a grafting or coating strategy, thereby improving comprehensive performance of polymeric membranes. However, most surface coating and surface grafting suffered flux reduction and unsustainability of the functional layer.[9] Alternatively, blending modification is another practical method without any pre- and post-treatment

18418

procedures compared to surface modification.[10] Recent advances in blending modification have opened up the possibility of integrating the advantages of inorganic fillers with the organic polymer, boosting membrane performance with higher permeability, selectivity, and antifouling properties compared with pristine polymeric membranes.[1,2] Currently, various inorganic nanoparticles, such as zeolites, metal oxide nanomaterials, carbon nanotubes, and graphene oxide (GO), have been investigated in an attempt to ameliorate membrane performance.[11−47] In particular, GO has gained increasing appeal due to its salient features, such as abundant oxygenous functional groups and fascinating mechanical and thermal properties,[48] which offer innovative alternatives for the development of hybrid membranes with unique structural properties, strong hydrophilicity, excellent selectivity without having to compromise permeability, and excellent antifouling properties.[49] Most recently, numerous efforts have been conducted to upgrade the performance of polymer/GO membranes in terms of hydrophilicity, mechanical strength, permeability, selectivity, etc.[50] However, GO, as well as other nanoparticles, has pinpointed an inherent dilemma encountered in blending modification: plenty of nanoparticles are embedded within the polymer matrix during the blending process, which cuts down the modification efficiency.[15] Therefore, it is a prevailing challenge to enrich the anchoring of nanoparticles on the membrane surface and thus engineer a robust antifouling membrane surface that can truly exploit the modification efficiency, rather than embedding nanoparticles within the polymer matrix or depositing nanoparticles on the membrane surface.

Previous reports have shown that application of a magnetic field during membrane preparation can oblige magnetic Fe_3O_4 particles to move along the magnetic field direction, contributing to improved water flux and rejection.[51] Hence, inspired by the movement of magnetic Fe_3O_4 particles in the casting solution under a magnetic field, the Fe_3O_4/GO−PVDF hybrid ultrafiltration membrane was prepared via the combination of magnetic field induced casting and a phase inversion technique in the present study. With this novel method, Fe_3O_4/GO nanocomposites migrate to the top surface of the membrane, stably enriching GO anchoring on the membrane surface rather than embedding GO within the polymer matrix; thus a robust antifouling membrane surface is engineered, avoiding from the instability of GO on GO−modified membrane surface and the coverage of GO in GO−blended composite membrane matrix. For this purpose, magnetic Fe_3O_4/GO nanocomposites were first synthesized via a facile one-step chemical coprecipitation method, in hopes of achieving the following practical advantages: (i) the amelioration of the aggregation tendency of nanoparticles and (ii) excellent magnetism for magnetic field induced casting while high hydrophilicity is kept. As a commonly used membrane material, PVDF was chosen to prepare the novel Fe_3O_4/GO−PVDF hybrid ultrafiltration membranes from the Fe_3O_4/GO/PVDF blends. The effects of Fe_3O_4/GO and magnetic induced casting on the structure, morphology, and performance of membranes were investigated carefully. Membrane characterizations were confirmed in terms of chemical composition, structural morphology, hydrophilicity, pure water flux, rejection, and others.

2. EXPERIMENTAL SECTION

2.1. Materials. GO was prepared via a modified Hummers' method through oxidation of graphite flakes (>99.95% purity, average diameter of 4 mm), and a more detailed procedure can be found in our earlier work.[47] PVDF (FR-904, Shanghai 3F New Materials Co., Ltd.) was dried at 80 °C for 12 h prior to use. N,N-Dimethylacetamide (DMAc) and polyvinylpyrrolidone (PVP) were supplied by Tianjin Kermel Chemical Co., Ltd. Bovine serum albumin (BSA, MW = 68 000) was the product of Beijing Biohao Biotechnology Co., Ltd. Ferrous chloride tetrahydrate ($FeCl_2·4H_2O$), ferric chloride hexahydrate ($FeCl_3·6H_2O$), 28% ammonium hydroxide (NH_4OH), 98% H_2SO_4, $KMnO_4$, 30% H_2O_2, and all other chemicals were purchased in analytical purity from Tianjin No. 3 Chemical Plant.

2.2. Preparation and Characterization of Fe_3O_4/GO Nanocomposites. Fe_3O_4/GO nanocomposites were synthesized according to a facile one-step chemical coprecipitation method with a slight modification.[52] In brief, GO (40 mg) was dispersed in a 100 mL three-neck flask containing 40 mL of distilled water for 3 h, followed by purging with nitrogen (N_2) for 30 min. A solution of $FeCl_2·4H_2O$ (124.3 mg) and $FeCl_3·6H_2O$ (186.4 mg) in water (5 mL) was purified with N_2 for 30 min before adding to the flask under continuous stirring in N_2 atmosphere. NH_4OH was added dropwise to the resulting mixture (with a temperature of 65 °C) to adjust the pH to 10. Then stirring of the mixture was maintained at 65 °C for an additional 3 h in N_2 atmosphere and then the mixture cooled to room temperature. Finally, the resultant precipitate was separated magnetically, washed thoroughly with ethanol and distilled water to neutral pH, and freeze-dried for 24 h to get Fe_3O_4/GO nanocomposites. For comparison, Fe_3O_4 nanoparticles were synthesized under the same conditions without the presence of GO.

The morphology, microstructure, magnetism, and compositions of nanocomposites were characterized by transmission electron microscopy (TEM) (FEI TecnaiG2F20), X-ray diffractometry (XRD) (D8 Discover), vibrating sample magnetometry (VSM) (MPMS), Fourier-transform infrared spectroscopy (FTIR) (TENSOR37), and X-ray photoelectron spectroscopy (XPS) (ESCALab 250).

2.3. Preparation of Membranes. The novel Fe_3O_4/GO−PVDF hybrid ultrafiltration membranes were developed from the Fe_3O_4/GO/PVDF blends via magnetic field induced casting and a phase inversion method similar to the method reported elsewhere.[51] Typically, the desired amounts of PVDF (15 g), Fe_3O_4/GO (1 g), and PVP (1 g) were dissolved in DMAc (83 g) under ultrasonication and agitation to generate a homogeneous casting solution, and the mixture was further continuously stirred at 50 °C for 24 h. After release of the air bubbles and cooling to room temperature, the solution was casted in air (25 ± 1 °C, relative humidity 30−40%) onto a glass plate in an open vessel with a magnetic field (0.1−0.2 T), the direction of which was horizontal to the glass plate at a distance of 4.0 cm. After a 25−30 s delay, distilled water was poured into the vessel to complete the immersion−precipitation process. Finally, the resultant membranes were soaked in distilled water for further utilization. For comparison, Fe_3O_4/GO−PVDF membranes without magnetic field induced casting, Fe_3O_4−PVDF membranes with and without magnetic field induced casting, GO−PVDF, and pristine PVDF membranes were prepared by the same process following the recipes in Table 1.

Table 1. Compositions of Vaious Membranes

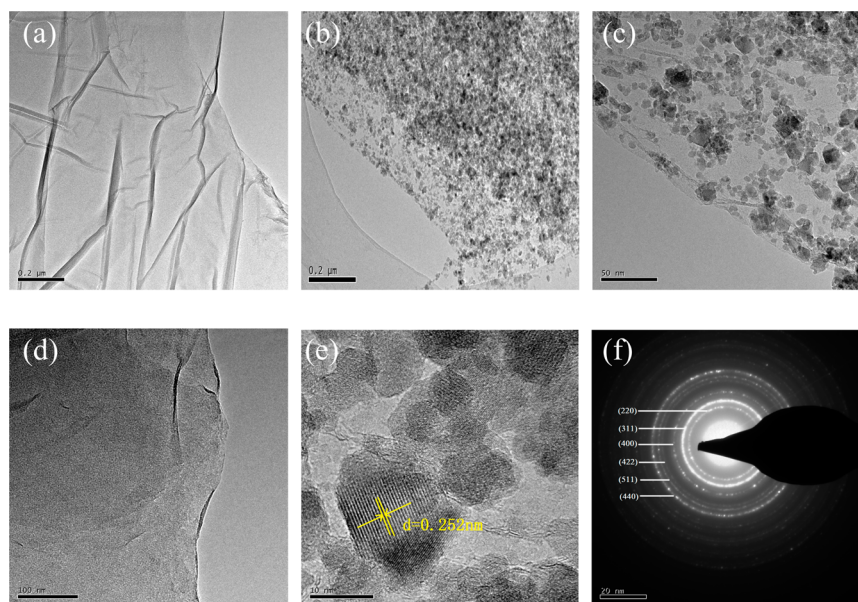| name	PVDF (wt %)	PVP (wt %)	nanomaterials (1 wt %)	DMAc (wt %)	magnetic field
PVDF	15	1	−	84	no
GO	15	1	GO	83	no
Fe_3O_4	15	1	Fe_3O_4	83	no
M-Fe_3O_4	15	1	Fe_3O_4	83	yes
Fe_3O_4/GO	15	1	Fe_3O_4/GO	83	no
M-Fe_3O_4/GO	15	1	Fe_3O_4/GO	83	yes

Figure 1. TEM images of GO (a) and Fe_3O_4/GO nanocomposites (b, c), HRTEM images of GO (d) and Fe_3O_4/GO nanocomposites (e), and (f) selected area electron diffraction (SAED) pattern of Fe_3O_4/GO nanocomposites.

2.4. Characterization of Membranes. To investigate how Fe_3O_4/GO nanocomposites are dispersed within the hybrid membranes, two kinds of composition analysis were carried out. For the first kind of composition analysis, energy dispersive X-ray spectroscopy (EDS) coupled with scanning electron microscopy (SEM) (Hitachi S-4800) was performed to determine the elemental composition and to the analyze elemental distribution. For the second kind of composition analysis, XPS at different takeoff angles (45° and 90°) was performed to study the near-surface compositions of membranes. Elemental analysis (EA) (Flash 2000) was performed to probe the whole elemental content of the membrane matrix. The atomic ratio of oxygen in the near-surface (O_{sur}) to that in the membrane matrix (O_{mat}) was used to evaluate the migration behavior of Fe_3O_4/GO in membranes, as the oxygen is the major element of Fe_3O_4/GO nanocomposites (the iron cannot be characterized by EA). In order to study the stability of Fe_3O_4/GO in the membrane matrix during the membrane filtration, ultrapure water was filtered through hybrid membranes for 3 h. The penetrating water was collected every 30 min. Iron concentrations in the penetrating water were measured using inductively coupled plasma optical emission spectroscopy (ICP-OES) (Vista 715-ES, Varian) with argon as carrier gas. Meanwhile, XPS was used to investigate the presence of Fe_3O_4/GO nanoparticles before and after membrane filtration.

The membrane morphology was characterized by SEM after the samples were fractured in liquid nitrogen and gold-sputtered. The membrane surface roughness was characterized by atomic force microscopy (AFM) (CSPM5500) in noncontact mode. Roughness parameters such as root-mean-square roughness (RMS) and mean roughness (Ra) were quantified from the topography images of 8 μm × 8 μm area. The membrane porosity was determined using the gravimetric method,[45] and mean pore size was investigated by the bubble point method using a capillary flow porometer (PMI, Ithaca, NY). The membrane hydrophilicity was conducted using a contact angle goniometer (JC2000D1). Pure water flux and rejection tests were measured following the procedure described in our previous report [a detailed description is provided in the Supporting Information (SI)].[47] Both the pure water flux and rejection tests were conducted at 0.1 MPa and 25 °C. Prior to water flux testing, the membranes were pressurized at 0.15 MPa for 1 h to obtain a stable water flux.[53] All the reported data were based on at least five repeats.

2.5. Antifouling Tests of Membranes. For the fouling resistance analysis, the experiments including three filtration steps were conducted and based on the procedure described in our previous

paper.[47] In brief, the pure water permeability (J_{w_1}) was measured until the flux remained stable in the first step. Then, the BSA flux (J_p) was measured for 1 h when using 1.0 g L^{-1} BSA solution to replace pure water. Then the membranes were washed with distilled water for 30 min to remove pollutant before measuring the water flux (J_{w_2}).

To further investigate the fouling process, the flux recovery ratio (FRR), the total fouling ratio (R_t), reversible fouling ratio (R_r), and irreversible fouling ratio (R_{ir}) were determined as follows:[54,55]

$$FRR\ (\%) = \frac{J_{w_2}}{J_{w_1}} \times 100 \tag{1}$$

$$R_t\ (\%) = \left(1 - \frac{J_p}{J_{w_1}}\right) \times 100 \tag{2}$$

$$R_r\ (\%) = \left(\frac{J_{w_2} - J_p}{J_{w_1}}\right) \times 100 \tag{3}$$

$$R_{ir}\ (\%) = \left(\frac{J_{w_1} - J_{w_2}}{J_{w_1}}\right) \times 100 = R_t - R_r \tag{4}$$

In addition, the interaction forces between membrane surface and foulants were quantified by an AFM method, where BSA, which served as a model foulant, was immobilized on the cantilever based on the procedure described in our previous publications (details are presented in the SI).[38] The AFM was performed in contact mode. To minimize the experimental error and to determine the force distribution, about 50 approach/retraction cycles were conducted on the membrane surface for at least five locations, with 20 measurements at each location.

3. RESULTS AND DISCUSSION

3.1. Structural Morphology and Magnetism of Fe_3O_4/ GO Nanocomposites. The morphology of GO and Fe_3O_4/ GO nanocomposites were illustrated by TEM, as seen in Figure 1. For GO, the transparency of the GO sheet suggested that the graphite oxide was well-exfoliated into few-layer GO nanosheets. For Fe_3O_4/GO, a large number of spherical Fe_3O_4
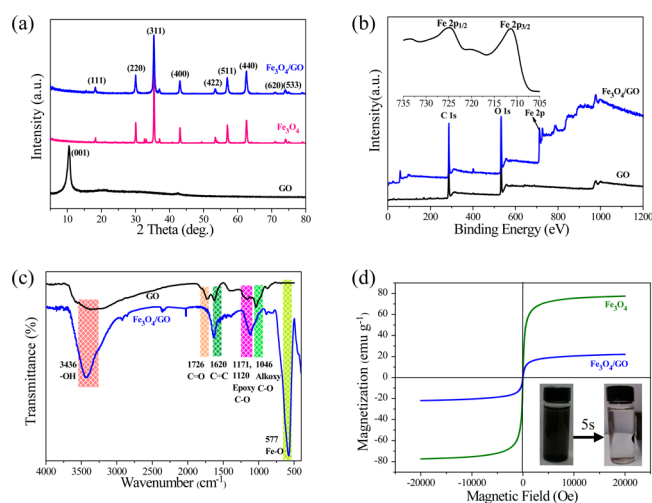
Figure 2. (a) XRD patterns of GO, Fe_3O_4, and Fe_3O_4/GO nanocomposites; (b) XPS spectra of GO and Fe_3O_4/GO nanocomposites, where the inset shows the Fe 2p spectrum of Fe_3O_4/GO nanocomposites; (c) FTIR spectra of GO and Fe_3O_4/GO nanocomposites; (d) magnetization hysteresis loops of Fe_3O_4 and Fe_3O_4/GO nanocomposites at room temperature, where the inset shows the photographs of Fe_3O_4/GO nanocomposites in water and their response to an external magnetic field within 5 s.

nanoparticles were randomly distributed on the surface of GO nanosheets, distinguishable in the low-magnification TEM images (Figure 1b,c). The corresponding high-magnification (HRTEM) image (Figure 1e) revealed that the (311) crystal lattice spacing of Fe_3O_4 was around 0.252 nm, suggesting the cubic structure.[57,59] Moreover, the SAED pattern (Figure 1f) of Fe_3O_4/GO nanocomposites revealed the highly crystalline reflections of the cubic Fe_3O_4 structure, which coincided with the XRD result. The Fe_3O_4 nanoparticles that were attached onto the surface of GO nanosheets may hinder the restacking of GO nanosheets, while the wimple structure of GO nanosheets may decrease the aggregation of Fe_3O_4 nanoparticles,[56] which will be beneficial for the compatibility between Fe_3O_4/GO and ploymer matrix.

The XRD patterns of GO, Fe_3O_4, and Fe_3O_4/GO are shown in Figure 2a. The peak around 10° for GO was related to the (001) interlayer structure of GO nanosheets. For Fe_3O_4, the diffraction peaks at 18.3°, 30.0°, 35.4°, 36.7°, 43.3°, 53.5°, 57.0°, 62.8°, 71.0°, and 74.4° can be indexed to the cubic crystal structure,[62] consistent with the HRTEM result (Figure 1e). The XRD pattern of Fe_3O_4/GO nanocomposites showed no obvious differences with that of Fe_3O_4, while no (001) diffraction of GO was observed, thus implying that the regular stack of GO may be destroyed by the intercalation of Fe_3O_4
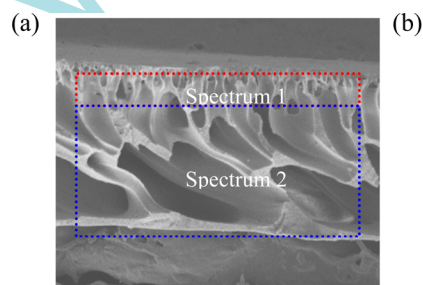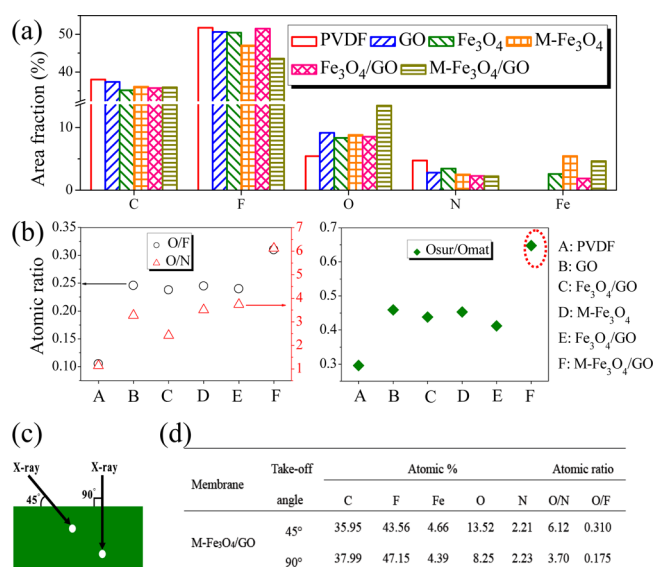

Figure 4. XPS results of various membranes. (a) Area fractions of C, F, Fe, O, and N relative to the sum of these elements present at the surface of various membranes as determined by XPS spectra with a takeoff angle of 45°. (b) O/F (circles), O/N (triangles), and Osur/Omat (diamonds) atomic ratios of various membranes. The values of O/F and O/N were obtained from XPS survey scans with a takeoff angle of 45°. Osur was the value of O at the surface of various membranes determined by XPS spectra with a takeoff angle of 45°. Omat was the values of O in the matrix of various membranes determined by EA. (c) The scheme for modifying the analysis depth of XPS measurement by adjusting the takeoff angle. (d) The elemental composition of M-Fe_3O_4/GO membranes determined by XPS spectra with the takeoff angle of 45° and 90°.
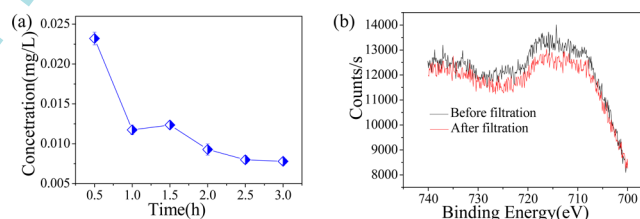
Figure 5. Stability of Fe_3O_4/GO in membranes: (a) concentration of leaching Fe in the permeate flux filtrated by M-Fe_3O_4/GO membranes and (b) XPS spectra of the surface for M-Fe_3O_4/GO membranes before and after filtration.

nanoparticles.[58] The chemical composition of GO and Fe_3O_4/GO nanocomposites was characterized by XPS, as the wide-survey XPS spectra is depicted in Figure 2b. For Fe_3O_4/GO, the three main peaks can be associated with C 1s, O 1s, and Fe

Figure 3. (a) Schematic illustration of element detection and (b) the corresponding results of various membranes by SEM–EDS.

Figure 6. SEM images of a typical M-Fe$_3$O$_4$/GO membrane: (a) cross-sectional morphology, (b) inner structure, (c) top surface morphology, (d) bottom surface morphology, and (e) the corresponding EDS mapping scanning spectra of C, O, and Fe on the membrane surface.

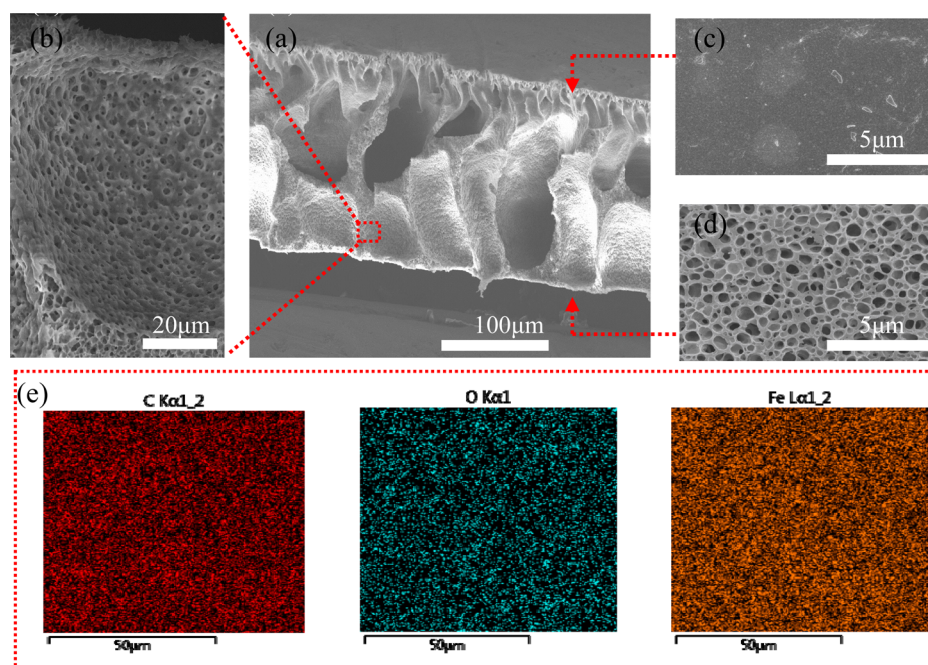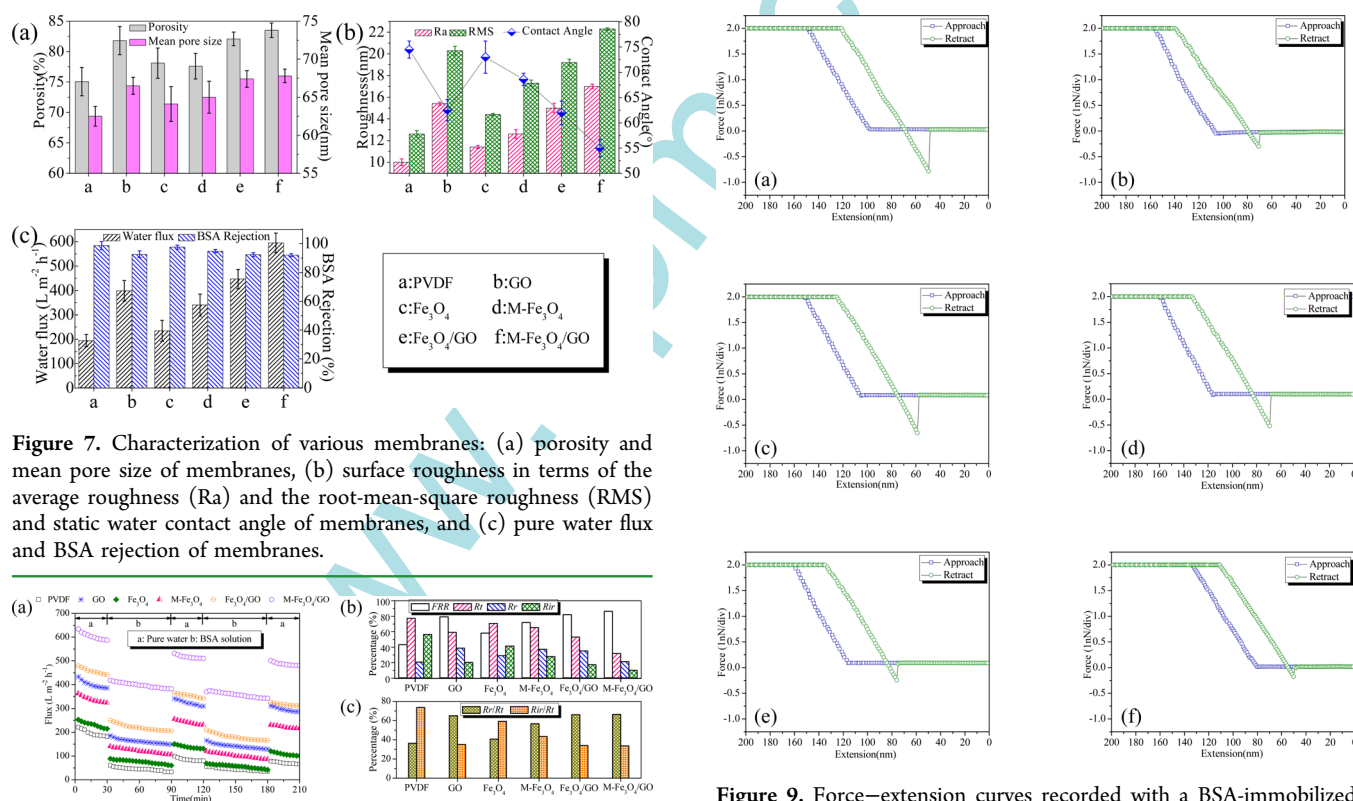**Figure 7.** Characterization of various membranes: (a) porosity and mean pore size of membranes, (b) surface roughness in terms of the average roughness (Ra) and the root-mean-square roughness (RMS) and static water contact angle of membranes, and (c) pure water flux and BSA rejection of membranes.

Figure 8. Antifouling properties of membranes: (a) time-dependent flux of various membranes under two cycles of BSA solution filtration, (b) water flux recovery and fouling resistance ratio of membranes, and (c) the ratio of reversible fouling (Rr) and irreversible fouling (Rir) to the total fouling ($Rt = Rr + Rir$), respectively.

Figure 9. Force−extension curves recorded with a BSA-immobilized tip against various membrane surfaces: (a) PVDF, (b) GO, (c) Fe$_3$O$_4$, (d) M-Fe$_3$O$_4$, (e) GO/Fe$_3$O$_4$, and (f) M-GO/Fe$_3$O$_4$.

2p, respectively. In the spectrum of Fe 2p (inset of Figure 2b), the peaks at 711.4 and 726.3 eV correspond to Fe 2p3/2 and Fe 2p1/2 in Fe$_3$O$_4$, respectively.[61] Additionally, the decreased

intensity for the C 1s XPS spectrum of Fe$_3$O$_4$/GO nanocomposites indicated partial reduction of GO (see Figure S2, SI).[59] Furthermore, the FTIR spectra presented in Figure 2c were recorded to characterize further the Fe$_3$O$_4$/GO nanocomposites. As expected, the FTIR spectrum of GO is well-consistent with previous works.[47] Compared with that of GO, the new band at 577 cm^{-1} of Fe$_3$O$_4$/GO nanocomposites can

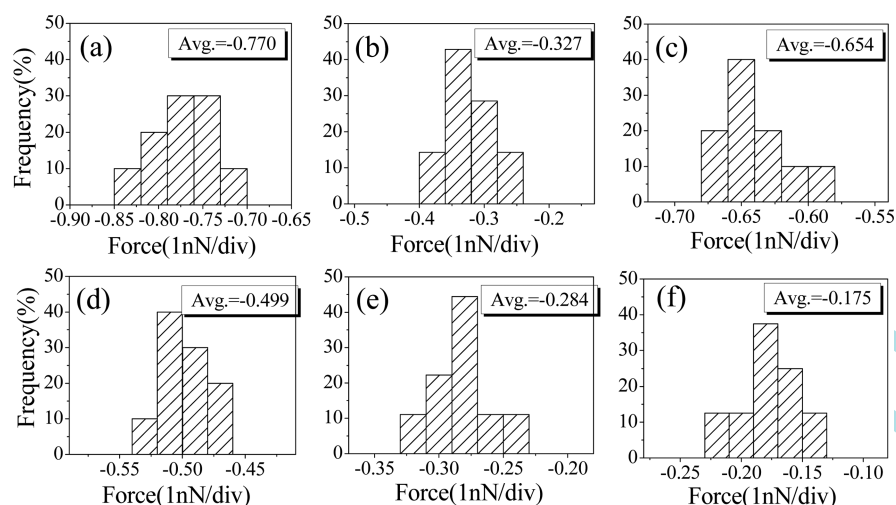**Figure 10.** Representative frequency distribution values of the corresponding interaction forces from 20 measurements between BSA-immobilized tip and various membranes: (a) PVDF, (b) GO, (c) Fe_3O_4, (d) $M-Fe_3O_4$, (e) GO/Fe_3O_4, and (f) $M-GO/Fe_3O_4$.

be assigned to the lattice absorption of Fe_3O_4, confirming the interaction of the Fe_3O_4 with the ester O.[56] As shown in Figure 2d, the magnetic performance of the Fe_3O_4/GO was characterized using VSM. The saturation magnetization of the Fe_3O_4/GO sample was 23.5 emu g^{-1}, indicating a high magnetism. Taken together, all the characterization results illustrated the successful synthesis of Fe_3O_4/GO nanocomposites.

3.2. Migration Behavior of Fe_3O_4/GO in Membranes. To investigate the migration behavior of Fe_3O_4/GO nanocomposites in membranes, EDS was applied to determine the elemental composition and analyze elemental distribution in the cross section of membranes. According to Figure 3a, two regions of the cross-section of membranes were subjected to EDS. A section across the top skin layer (spectrum 1) and a section across the sublayer (spectrum 2) were sampled. It could be seen that there was still oxygen detected in pristine PVDF membrane, which was mainly due to the remnant of PVP in the membranes. The same experience was also confirmed by Chang et al.[34] and Qin et al.[60] Compared with pristine PVDF membranes, the increment in O content could be noted for Fe_3O_4 and Fe_3O_4/GO membranes, but it was not as palpable as for $M-Fe_3O_4$ and $M-Fe_3O_4/GO$ membranes. For $M-Fe_3O_4$ and $M-Fe_3O_4/GO$ membranes, the significant increment in oxygen content of the membrane surface could be interpreted as the migration of magnetic nanomaterials toward membrane surfaces with the aid of the magnetic field during the membrane formation. Moreover, the oxygen content in spectrum 1 for $M-Fe_3O_4$ and $M-Fe_3O_4/GO$ membranes was about 56% and 97% higher than that in spectrum 2, respectively, verifying the benefit of magnetic field induced casting on the surface enrichment of magnetic nanomaterials. Furthermore, digital pictures of both sides of various membranes are represented in Figure S9 (SI). It could be found that the color of the top surface was darker than the bottom side for $M-Fe_3O_4/GO$ membranes, confirming the surface enrichment of Fe_3O_4/GO nanocomposites, which was is in accordance with the conclusion drawn from Figure 3.

Similar trends were found when comparing the surface elemental compositions (Figure S7, SI) and the corresponding surface elemental mole percentages of membranes (Figure 4a). Apparently, oxygen, one of the dominating elements of

hydrophilic nanomaterials, for all the hybrid membranes was higher than for pristine PVDF membranes (details are presented in Figure S8, SI). For further demonstration, the atomic ratios of oxygen to fluorine (O/F) and oxygen to nitrogen (O/N) were calculated, as depicted in Figure 4b. The atomic ratios of O/F and O/N were increased from 0.105 and 1.14 for pristine PVDF membranes to 0.240 and 3.74 for Fe_3O_4/GO membranes and then increased to 0.310 and 6.12 for $M-Fe_3O_4/GO$ membranes, indicating the surface enrichment of Fe_3O_4/GO nanocomposites. Additionally, on the basis of the O_{sur}/O_{mat} ratios obtained by XPS and EA, it could be found that the atom ratio of O_{sur}/O_{mat} for $M-Fe_3O_4/GO$ membranes was 0.648, being 2.2 times and 1.5 times higher than that of PVDF membranes (0.296) and Fe_3O_4/GO membranes (0.412), respectively, indicating the distinct surface enrichment of $M-Fe_3O_4/GO$ membranes. Moreover, the surface elemental compositions of $M-Fe_3O_4/GO$ membranes at different depth levels were analyzed using XPS with a takeoff angle of 45° and 90°, and the results are tabulated in Figure 4d. As the takeoff angle increases, sampling depth increases (Figure 4c).[9] As can be seen from Figure 4d, the atomic percentage of oxygen element of $M-Fe_3O_4/GO$ membranes decreased from 13.52 at 45° to 8.25 at 90°, suggesting the higher relative amount of oxygen in the near-surface of $M-Fe_3O_4/GO$ membranes (i.e., the higher amount of Fe_3O_4/GO nanocomposites).

Therefore, it can be safely concluded that the Fe_3O_4/GO nanocomposites could migrate and be anchored on the membrane surface via magnetic field induced casting, which is advantageous to the amelioration of membrane hydrophilicity and antifouling properties.

3.3. Stability of Fe_3O_4/GO in Membranes. In order to probe the stability of Fe_3O_4/GO in membrane matrix during the membrane filtration, ICP-OES was evaluated to quantitatively analyze the extent of Fe_3O_4/GO leaching during the membrane filtration. As depicted in Figure 5a, the iron concentration that leached from the $M-Fe_3O_4/GO$ membranes was very low (only 0.023 208 mg/L in the permeate flux for 30 min) and decreased as more water filtrated with the increasing time (0.00784 mg/L in the permeate flux for 3 h), indicating the stability of Fe_3O_4/GO in the membrane matrix during the membrane filtration. Meanwhile, XPS was conducted to

Table 2. Comparison of the Comprehensive Performance of the as-Prepared Hybrid Membranes in This Work against Different Inorganic Nanomaterial−Polymer Hybrid Membranes from the Recent Literature

membrane	optimum dosage (wt %)	contact angle (deg)	water permeability (L m^{-2} h^{-1} bar^{-1})	BSA rejection (%)	water flux recovery (%)	ref
PVC−ZnO[a]	3	54.5	201	97.5	91.8	21
PES−ZnO[a]	0.1	55.9	∼300	∼95	64	20
PES−ZrO$_2$[a]	1	52.3	83.6	92.7	∼95	13
PES−SiO$_2$[b]	5	−	141.8	94.6	84.4	14
PES−ZIF-L[a,d]	0.5	∼62	378	∼90	82	17
PVDF−Al$_2$O$_3$[a]	2	81.1	134.4	93.4	∼40	19
PVDF−Fe$_3$O$_4$[b]	25	−	65.6	93	55.2	11
PVDF−TiO$_2$[b]	25	∼64	150	−	∼93	15
PVDF−TiO$_2$[b]	20	60.7	103.5	85.6	96.9	16
PVDF−APT[b,e]	7	63	401.2	88.7	75.1	18
CA−TiSiO$_4$[b]	20	56.6	67.2	∼92	85.7	12
BPPO−MWCNTs[b]	5	62.8	487	94	−	22
PAN−MWCNTs[a]	0.5	∼43	∼34	∼86	−	29
PES−MWCNTs[a]	0.4	∼50	∼2	−	77.2	24
PES−MWCNTs[a]	1	65	∼18.8	95	−	25
PES−MWCNTs/TiO$_2$[a]	1	56.1	5.66	−	78.4	26
PES−PEGMA−CNTs[a]	3	51.2	272.8	75.4	98	27
PES−NH$_2$−MWCNTs[a]	0.045	55.5	∼6	−	100.2	28
PVDF−MWCNTs[a]	1	53	620	89	−	36
PVDF−MWCNTs[b]	1.5	75	∼8	90.4	92.5	23
PVDF−OMWCNTs[a]	0.3	100.1	230.7	75.8	65.7	30
PVDF−OMWCNTs[a]	1	66.8	119	86.9	72.8	37
PA−GO[a]	0.2	65	∼6	−	∼95	31
PS−GO[c]	0.005	69.2	70	∼75	−	46
BPPO−PEI−GO[b]	0.6	−	532	91	64	33
PSF−GO[a]	1.3	82.5	∼430	−	−	32
PSF−iGO[a]	0.05	∼80	140	95	40.3	43
PSF−SiO$_2$/GO[a]	0.3	∼62	∼185	98	72	44
PES−GO[a]	0.5	53.2	5.1	96	90.5	35
PES−HPEI−GO[a]	5	63.1	153.5	∼92	88.7	42
PVDF−GO[a]	0.5	∼68	104.3	85	−	34
PVDF−GO[a]	0.2	60.7	457.9	91.1	96.4	40
PVDF−GO[b]	2	60.5	26.5	−	88.6	41
PVDF−GO[c]	2	58.8	467.8	67.6	85.7	47
PVDF−GO[a]	1	68	505	87.0	−	36
PVDF−GO[a]	1	51	401.4	55	98	38
PVDF−GO[a]	1	66.4	163	83.7	85.1	37
PVDF−GO/OMWCNTs[a]	1	48.6	203	81.6	80.4	37
PVDF−PDAAQ/rGO[b]	1.5	69.8	∼68	77.4	86.8	39
PVDF−rGO/TiO$_2$[b]	0.05	69	73.7	99	95	45
GO[a]	1	62.5	398.7	92.6	79.3	this work
Fe$_3$O$_4$[a]	1	73	234.4	97.6	58.2	
M-Fe$_3$O$_4$[a]	1	68.6	346.6	94.9	71.8	
Fe$_3$O$_4$/GO[a]	1	62	446.7	92.4	82.1	
M-Fe$_3$O$_4$/GO[a]	1	55	595.4	92.0	86.4	

[a]The dosage of inorganic nanomaterials is based on the total weight of polymer casting solution. [b]The dosage of inorganic nanomaterials is based on the weight of polymer. [c]The dosage of inorganic nanomaterials is based on the concentration of the coagulation bath. [d]ZIF-L: Zeolitic imidazolate framework with leaf-shaped morphology. [e]APT: Attapulgite.

investigate the presence of Fe$_3$O$_4$/GO nanoparticles during the membrane filtration. As shown in Figure 5b, the peak intensity of Fe element of M-Fe$_3$O$_4$/GO membranes was still obvious after filtration, suggesting the stability of Fe$_3$O$_4$/GO in the membrane matrix during the membrane filtration. In order to probe the exact amount of Fe$_3$O$_4$/GO in the whole membrane, ICP-OES was evaluated to quantitatively analyze the concentration of Fe$_3$O$_4$ in the coagulation bath (4 L of water) used for the complete nonsolvent-induced phase separation. After 15 days, the leaching amounts of Fe$_3$O$_4$ into

water were measured as 4 mg/L. Then the Fe$_3$O$_4$/GO leaching from the membrane during the nonsolvent-induced phase separation process was calculated as around 33 mg according to the content of Fe$_3$O$_4$ in Fe$_3$O$_4$/GO nanocomposites, and the retained amount of Fe$_3$O$_4$/GO in membrane was around 0.967g, which is near to the nominal value (1 g) used for the preparation of membranes.

3.4. Morphology and Structure of Membranes. The top, bottom, and cross-section views of membranes are compared in Figure 6 (and Figures S6, S10, and S11, SI). All

the membranes showed a typical asymmetric microstructure, including a dense skin layer supported by numerous macrovoids (sublayer). No distinct variations in the top and bottom surface of membranes were observed (Figure 6c,d). All the top surfaces seemed to be flat and smooth, while the bottom surfaces appeared macroporous, indicating that the structures of the top surface and bottom surface were not altered by the addition of inorganic nanomaterials. However, with the supplementation of GO, Fe_3O_4, and Fe_3O_4/GO into the polymer matrix, the cross section of various membranes formed wider pore channels, compared with pristine PVDF membranes (Figure 6a). Instantaneous liquid−liquid phase demixing is responsible for the amelioration of macrovoid formation.[61] For M-Fe_3O_4/GO membranes, the macroporous inner structures (Figure 6b) and enlarged macrovoids compared with Fe_3O_4/GO membranes could be visually observed, indicating that the magnetic field induced casting during the membrane preparation benefited the water permeability.[11] Furthermore, SEM−EDS mapping scanning spectra of the membrane surface of carbon, oxygen, and iron elements were collected out to explore the presence and distribution of Fe_3O_4/GO nanocomposites on the membrane surface, as observed in Figure 6e. It is noted that the Fe element uniformly distributed on membrane surface, indicating the uniformity of Fe_3O_4/GO nanocomposites on the membrane surface.

The results of overall porosity and mean pore size of membranes are exhibited in Figure 7a (and Figure S12, SI). With the supplementation of inorganic nanomaterials, the pore size and porosity of membranes increased, especially for M-Fe_3O_4/GO membranes. This phenomenon could be interpreted as the rapid demixing process due to the significantly improved hydrophilic characteristic of M-Fe_3O_4/GO membranes compared with other membranes. Correspondingly, the M-Fe_3O_4/GO membranes presented an advantageous porous surface, which benefited for membrane permeability. Note that the mean pore size and porosity of the Fe_3O_4 and M-Fe_3O_4 membranes were lower than those of GO hybrid membranes. The poor hydrophilicity of Fe_3O_4 and M-Fe_3O_4 membranes compared with GO hybrid membranes may be responsible for this behavior,[61] which is consistent with the results of contact angles (Figure 7b) and is also verified by the oxygen content of membranes determined by EA and XPS (Table S1, SI).

AFM was also used to investigate the membrane surface, as demonstrated in Figure 7b (and Figure S13, SI). According to the AFM images and the corresponding roughness parameters presented in Figure 7b, the surface roughness of the hybrid membranes, employing Ra and RMS, displayed a slightly increasing trend compared with that of pristine PVDF membranes. Under a scan range of 8 μm × 8 μm, the Ra value increased from 10.0 nm (PVDF) to 15.4 nm (GO), 11.4 nm (Fe_3O_4), 12.6 nm (M-Fe_3O_4), 15.0 nm (Fe_3O_4/GO), and 17.0 nm (M-Fe_3O_4/GO), which was possibly due to the presence of inorganic nanomaterials on the surfaces of the hybrid membranes. It is generally deemed that a membrane with smoother surface possesses better antifouling characteristics.[62] However, if the high roughness is the outcome of the surface enrichment of hydrophilic nanomaterials, it enhances the membrane hydrophilicity significantly, despite its high roughness.[63] Therefore, the hybrid membranes have potential antifouling tendency.

3.5. Hydrophilicity and Filtration Properties of Membranes. Surface hydrophilicity is a significant factor affecting the filtration properties of membranes. The membrane

hydrophilicity was understood on the basis of water contact angle measurement.[47] In general, a smaller contact angle refers to a higher hydrophilicity. Compared in Figure 7b are the static contact angle results of membranes. Supplementation of the membrane with GO, Fe_3O_4, and Fe_3O_4/GO tended to considerably decrease the water contact angle. Pristine PVDF membranes possessed the highest contact angle of 74.5°, whereas GO, Fe_3O_4, M-Fe_3O_4, Fe_3O_4/GO, and M-Fe_3O_4/GO hybrid membranes achieved water contact angles of 62.5°, 73.0°, 68.6°, 62.0°, and 55.0°, respectively. The amelioration of hybrid membrane hydrophilicity may be ascribed to the spontaneous migration of hydrophilic nanomaterials moving toward the membrane/water interface to decrease the interface energy during the membrane formation.[11,50] Note that the contact angle of M-Fe_3O_4 and M-Fe_3O_4/GO membranes was slightly smaller than that of Fe_3O_4 and Fe_3O_4/GO membranes. The migration and enrichment of magnetic nanoparticles on membrane and pore surfaces with the aid of the magnetic field during the membrane preparation process may be responsible for this behavior.[51] Consequently, the improved hydrophilicity undoubtedly acted favorably in promoting water permeability and antifouling properties (discussed later).

The results of membrane performance concerning the pure water permeation flux and BSA rejection are also illustrated in Figure 7, which exhibits a similar trend that all hybrid membranes supplemented with inorganic nanomaterials possessed higher water fluxes without having a compromise in BSA rejection as compared to pristine PVDF membranes. In marked contrast, the water flux of M-Fe_3O_4/GO membranes was 595.39 L m^{-2} h^{-1}, being 206%, 49%, and 33% higher than that of PVDF (194.60 L m^{-2} h^{-1}), GO (398.74 L m^{-2} h^{-1}), and Fe_3O_4/GO membranes (446.74 L m^{-2} h^{-1}), respectively. This improvement in water flux may result from the coupling effects of the following two main parameters: (1) Migration and enrichment of Fe_3O_4/GO nanocomposites on membrane and pore surfaces with the aid of a magnetic field during the membrane preparation would make the membrane more hydrophilic, which facilitates the water molecules to pass through the membrane.[11,50] It can be seen from Figure 7b that the declining trend of contact angle was in accord with water permeability promotion. (2) The formation of advantageous porous surfaces of M-Fe_3O_4/GO membranes (mentioned in section 3.4) was also responsible for water permeability promotion. Considering the results of pore size and porosity of membranes presented in Figure 7a (and Figure S12, SI), the M-Fe_3O_4/GO membranes displayed an increase in pore size and porosity as compared to other membranes, which undoubtedly benefited the water permeability.[64] Hence, the increased hydrophilicity, together with the bigger pores and higher porosity, enabled the M-Fe_3O_4/GO membranes to present superior water flux than the other control membranes. The results of BSA rejection are also presented in Figure 7c. As can be seen, the rejections of all membranes were more than 92%, indicating that the pore size of the skin layer of the membranes was smaller than the size of BSA.[54] It may be mentioned that the BSA rejection presented the decline trend with the supplementation of nanoparticles. The formation of a cake layer because of the interaction between the hydropholic surface of the membranes and BSA protein may lead to the increased BSA rejection, which has a negative effect on water permeability.

3.6. Antifouling Properties of Membranes. *3.6.1. Fouling Evaluation of Membranes.* The fouling behavior toward

various membranes was evaluated using dynamic filtration experiments, and the results are depicted in Figure 8. Figure 8a traced the typical time-dependent fluxes of various membranes in the two cycles of BSA solution filtration.[47] The hybrid membranes showed higher fluxes as compared to pristine PVDF membranes due to the improved hydrophilicity and higher surface porosity of the hybrid membranes. When the pure water was changed to BSA solution, flux declined sharply in BSA due to fouling. Nevertheless, the M-Fe$_3$O$_4$/GO membranes showed lower flux reduction coefficient and the highest permeation flux of the BSA solution due to the improved hydrophilicity. With simple water rinsing, the permeate flux of membranes was recovered in varying degrees, but it was not exactly reverted for all membranes. This may be ascribed to the BSA blocking membrane pores, in agreement with the experience of Damodar et al.[65] and Moghadam et al.[16] Nonetheless, a maximum improvement in flux recovery was presented for M-Fe$_3$O$_4$/GO membranes, indicating better antifouling performance over that of the other membranes. Moreover, this high water flux recovery was consistently obtained further on in the filtration cycle, suggesting that the antifouling characteristics of M-Fe$_3$O$_4$/GO membranes are stable in long-term operation.

Water flux recovery ratio (FRR) and fouling resistance ratios (R_t, R_r, and R_{ir}) were introduced and evaluated by employing eqs 1−4 to monitor membrane fouling, as illustrated in Figure 8b. Generally, a higher FRR value refers to a superior antifouling character of membranes. As can be clearly seen from Figure 8b, FRR of all hybrid membranes was significantly higher as compared to pristine PVDF membranes. This indicated the improved antifouling characteristic of the hybrid membranes. FRR of pristine PVDF membranes was as low as 43.3%, suggesting the poor antifouling property. When cast with no magnetic field, supplementation of the membrane with GO, Fe$_3$O$_4$, and Fe$_3$O$_4$/GO tended to considerably increase the FRR of the hybrid membranes, and the maximum FRR value (82.1%) was observed for Fe$_3$O$_4$/GO membranes. The amelioration of antifouling behaviors of the hybrid membranes can be attributed to the improved membrane morphology (mentioned in section 3.4) and membrane hydrophilicity compared with those of pristine PVDF membranes. Compared with the hybrid membranes without magnetic field induced casting, FRR for the hybrid membranes with magnetic field induced casting further increased, demonstrating that the surface migration of the hydrophilic inorganic nanomaterials endowed the membrane with antifouling tendency. Furthermore, R_t ($R_t = R_r + R_{ir}$) of all hybrid membranes was obviously lower than that of pristine PVDF membranes, concurring with permeability and hydrophilicity trends. In the best case, related to the M-Fe$_3$O$_4$/GO membranes, R_t decreased to 31.5%, suggesting the enhanced hydrophilicity of the membrane surface as a result of the migration of Fe$_3$O$_4$/GO nanocomposites.

In more detail, the membrane fouling was mainly associated with reversible resistance and irreversible resistance.[47] As shown in Figure 8c, R_r/R_t values were 26.4%, 65.0%, 40.7%, 56.7%, 66.1%, and 66.4% for PVDF, GO, Fe$_3$O$_4$, M-Fe$_3$O$_4$, Fe$_3$O$_4$/GO, and M-Fe$_3$O$_4$/GO membranes, respectively. On the contrary, R_{ir}/R_t of the hybrid membranes further decreased with magnetic field induced casting as compared to the hybrid membranes without magnetic field induced casting. The phenomena indicated that R_{ir} dominates the total fouling and that membrane fouling could be effectively mitigated by

enhancing membrane hydrophilicity. In summary, all of the obtained results indicated that the M-Fe$_3$O$_4$/GO membranes had better antifouling behavior over the other membranes.

3.6.2. Correlation between Fouling and Foulant−Membrane Interactions. Arising from the adhesion force measured by AFM between the membrane surface and foulants, the magnitude of the adhesion force was directly associated with the membrane fouling potential, which is a good indicator of membrane organic fouling.[66,67] Figure 9 shows the force−extension curves of various membrane surfaces, in which the inflection point in the retracting curve demonstrates the adhesion force between the membranes and BSA-immobilized tip.[68] Of note is that all measured negative values of the adhesive force only indicate the direction of the adhesive force.[69] As expected, the adhesion force between pristine PVDF and BSA was strong and reached to about −0.770 nN because of the hydrophobic interaction between the hydrophobic parts of BSA and hydrophobic PVDF.[70] Supplementation of the membrane with GO, Fe$_3$O$_4$, and Fe$_3$O$_4$/GO tended to decrease the interaction force. In particular, the adhesion force between M-Fe$_3$O$_4$/GO membranes and BSA was reduced considerably and reached to about −0.175 nN due to the surface migration of the hydrophilic Fe$_3$O$_4$/GO, which was in agreement with the surface elements analysis (mentioned in section 3.2).

Moreover, the frequency distributions of the adhesion force are presented in Figure 10. The magnitude of the adhesion force was consistent with the various characteristics of flux curves of membranes (Figure 8). It seems that the higher adhesion force leads to a more severe flux decline in filtration process, and vice versa, suggesting that the adhesion force measurement is a sensitive technique for predicting membrane fouling potential.[70]

Finally, the comprehensive performance of M-Fe$_3$O$_4$/GO membranes in this work was compared against different inorganic nanomaterial−polymer hybrid membranes from the recent literature, and the data are presented in Table 2. As can be clearly seen from the data, the M-Fe$_3$O$_4$/GO membranes presented an upgraded performance compared with the other inorganic nanomaterial−polymer hybrid membranes, which illustrates that such high-performance membranes have the distinct potential to be new-generation water filtration membranes.

4. CONCLUSIONS

In summary, a novel preparation method for Fe$_3$O$_4$/GO−PVDF hybrid membrane (M-Fe$_3$O$_4$/GO) was reported via the combination of magnetic field induced casting and a phase inversion technique. With this method, Fe$_3$O$_4$/GO nanocomposites migrate and anchor on the membrane top surface, which endows membrane with enhanced hydrophilicity and robust fouling resistant ability. The EDS analyses, where the oxygen content in the top skin layer was about 97% higher than that in the sublayer for M-Fe$_3$O$_4$/GO membranes, and the XPS and EA analyses, where the atomic ratio of oxygen in the near-surface compared to that in the membrane matrix for M-Fe$_3$O$_4$/GO membranes was about 1.5−2.2 times higher than that of PVDF and Fe$_3$O$_4$/GO membranes, showed the distinct migration and enrichment of the resultant Fe$_3$O$_4$/GO nanocomposites on membrane surface with the magnetic field induced casting. The ICP-OES and XPS analyses demonstrated the stability of Fe$_3$O$_4$/GO in the membrane matrix during the membrane filtration. As a result, the M-Fe$_3$O$_4$/GO hybrid membranes exhibited simultaneously upgraded hydrophilicity

(with a contact angle of 55.0°) and water flux (up to 595.39 L m^{-2} h^{-1}), which were improved by 26% and 206%, 12% and 49%, 25% and 154%, and 11% and 33% compared with those of pristine PVDF and PVDF hybrid membranes blended with GO, Fe_3O_4, and Fe_3O_4/GO without the assistance of magnetic field during membrane casting, respectively. Besides, the M-Fe_3O_4/GO hybrid membranes showed high rejection toward bovine serum albumin (>92%) and high flux recovery ratio (up to 86.4%) along with lower adhesion force between foulants and membrane surface compared with other membranes. Therefore, this study provides a reliable method for upgrading membrane performance by manipulating nanomaterial migration on a membrane surface rather than embedding them within a membrane matrix or depositing them on a membrane surface, thus highlighting a novel approach for advancing hybrid membranes with effectively reinforced permeation and antifouling performance. Additionally, this method can also be extended to more membrane materials prepared by the phase inversion technique.

■ ASSOCIATED CONTENT

Ⓢ Supporting Information

The Supporting Information is available free of charge on the ACS Publications website at DOI: 10.1021/acsami.6b04083.

> Detailed experimental description, the characterization of Fe_3O_4/GO nanocomposites, migration behavior of Fe_3O_4/GO in membranes, and the characterization of membranes (PDF)

■ AUTHOR INFORMATION

Corresponding Authors

*Z.X. e-mail: xuzhiwei@tjpu.edu.cn.
*X.Q. e-mail: qianxiaoming@tjpu.edu.cn.

Notes

The authors declare no competing financial interest.

■ ACKNOWLEDGMENTS

■ REFERENCES

(1) Goh, P.; Ng, B.; Lau, W.; Ismail, A. Inorganic Nanomaterials in Polymeric Ultrafiltration Membranes for Water Treatment. *Sep. Purif. Rev.* **2015**, *44* (3), 216−249.

(2) Yin, J.; Deng, B. Polymer-Matrix Nanocomposite Membranes for Water Treatment. *J. Membr. Sci.* **2015**, *479*, 256−275.

(3) Balta, S.; Sotto, A.; Luis, P.; Benea, L.; Van der Bruggen, B.; Kim, J. A New Outlook on Membrane Enhancement with Nanoparticles: the Alternative of ZnO. *J. Membr. Sci.* **2012**, *389*, 155−161.

(4) Kang, G. D.; Cao, Y. M. Application and Modification of Poly (vinylidene fluoride) (PVDF) Membranes-A Review. *J. Membr. Sci.* **2014**, *463*, 145−165.

(5) Hadidi, M.; Zydney, A. L. Fouling Behavior of Zwitterionic Membranes: Impact of Electrostatic and Hydrophobic Interactions. *J. Membr. Sci.* **2014**, *452*, 97−103.

(6) Baghbanzadeh, M.; Rana, D.; Lan, C. Q.; Matsuura, T. Effects of Inorganic Nano-Additives on Properties and Performance of Polymeric Membranes in Water Treatment. *Sep. Purif. Rev.* **2016**, *45* (2), 141−167.

(7) Ng, L. Y.; Mohammad, A. W.; Leo, C. P.; Hilal, N. Polymeric Membranes Incorporated with Mmetal/Metal Oxide Nanoparticles: A Comprehensive Review. *Desalination* **2013**, *308*, 15−33.

(8) Jhaveri, J. H.; Murthy, Z. A Comprehensive Review on Anti-fouling Nanocomposite Membranes for Pressure Driven Membrane Separation Processes. *Desalination* **2016**, *379*, 137−154.

(9) Liu, D.; Li, D.; Du, D.; Zhao, X.; Qin, A.; Li, X.; He, C. Antifouling PVDF Membrane with Hydrophilic Surface of Terry Pile-like Structure. *J. Membr. Sci.* **2015**, *493*, 243−251.

(10) Zhang, J.; Xu, Z.; Shan, M.; Zhou, B.; Li, Y.; Li, B.; Niu, J.; Qian, X. Synergetic Effects of Oxidized Carbon Nanotubes and Graphene Oxide on Fouling Control and Anti-fouling Mechanism of Polyvinylidene Fluoride Ultrafiltration Membranes. *J. Membr. Sci.* **2013**, *448*, 81−92.

(11) Huang, Z. Q.; Zheng, F.; Zhang, Z.; Xu, H. T.; Zhou, K. M. The Performance of the PVDF-Fe_3O_4 Ultrafiltration Membrane and the Effect of A Parallel Magnetic Field Used During the Membrane Formation. *Desalination* **2012**, *292*, 64−72.

(12) Dasgupta, J.; Chakraborty, S.; Sikder, J.; Kumar, R.; Pal, D.; Curcio, S.; Drioli, E. The Effects of Thermally Stable Titanium Silicon Oxide Nanoparticles on Structure and Performance of Cellulose Acetate Ultrafiltration Membranes. *Sep. Purif. Technol.* **2014**, *133*, 55−68.

(13) Pang, R.; Li, X.; Li, J.; Lu, Z.; Sun, X.; Wang, L. Preparation and Characterization of ZrO_2/PES Hybrid Ultrafiltration Membrane with Uniform ZrO_2 Nanoparticles. *Desalination* **2014**, *332* (1), 60−66.

(14) Zhu, L. J.; Zhu, L. P.; Jiang, J. H.; Yi, Z.; Zhao, Y. F.; Zhu, B. K.; Xu, Y. Y. Hydrophilic and Anti-fouling Polyethersulfone Ultrafiltration Membranes with Poly (2-hydroxyethyl methacrylate) Grafted Silica Nanoparticles as Additive. *J. Membr. Sci.* **2014**, *451*, 157−168.

(15) Méricq, J. P.; Mendret, J.; Brosillon, S.; Faur, C. High Performance PVDF-TiO_2 Membranes for Water Treatment. *Chem. Eng. Sci.* **2015**, *123*, 283−291.

(16) Moghadam, M. T.; Lesage, G.; Mohammadi, T.; Mericq, J. P.; Mendret, J.; Heran, M.; Faur, C.; Brosillon, S.; Hemmati, M.; Naeimpoor, F. Improved Antifouling Properties of TiO_2/PVDF Nanocomposite Membranes in UV-Coupled Ultrafiltration. *J. Appl. Polym. Sci.* **2015**, DOI: 10.1002/app.41731.

(17) Low, Z. X.; Razmjou, A.; Wang, K.; Gray, S.; Duke, M.; Wang, H. Effect of Addition of Two-dimensional Zif-L Nanoflakes on the Properties of Polyethersulfone Ultrafiltration Membrane. *J. Membr. Sci.* **2014**, *460*, 9−17.

(18) Zhang, Y.; Zhao, J.; Chu, H.; Zhou, X.; Wei, Y. Effect of Modified Attapulgite Addition on the Performance of A PVDF Ultrafiltration Mmembrane. *Desalination* **2014**, *344*, 71−78.

(19) Liu, F.; Abed, M. M.; Li, K. Preparation and Characterization of Poly (vinylidene fluoride) (PVDF) Based Ultrafiltration Membranes Using Nano γ-Al_2O_3. *J. Membr. Sci.* **2011**, *366* (1), 97−103.

(20) Zhao, S.; Yan, W.; Shi, M.; Wang, Z.; Wang, J.; Wang, S. Improving Permeability and Antifouling Performance of Polyethersulfone Ultrafiltration Membrane by Incorporation of ZnO-DMF Dispersion Containing Nano-ZnO and Polyvinylpyrrolidone. *J. Membr. Sci.* **2015**, *478*, 105−116.

(21) Rabiee, H.; Vatanpour, V.; Farahani, M. H. D. A.; Zarrabi, H. Improvement in Flux and Antifouling Properties of PVC Ultrafiltration Membranes by Incorporation of Zinc Oxide (ZnO) Nanoparticles. *Sep. Purif. Technol.* **2015**, *156*, 299−310.

(22) Wu, H.; Tang, B.; Wu, P. Novel Ultrafiltration Membranes Prepared from A Multi-walled Carbon Nanotubes/Polymer Composite. *J. Membr. Sci.* **2010**, *362* (1), 374−383.

(23) Zhao, X.; Ma, J.; Wang, Z.; Wen, G.; Jiang, J.; Shi, F.; Sheng, L. Hyperbranched-polymer Functionalized Multi-walled Carbon Nanotubes for Poly (vinylidene fluoride) Membranes: From Dispersion to Blended Fouling-control Membrane. *Desalination* **2012**, *303*, 29−38.

(24) Vatanpour, V.; Madaeni, S. S.; Moradian, R.; Zinadini, S.; Astinchap, B. Fabrication and Characterization of Novel Antifouling Nanofiltration Membrane Prepared from Oxidized Multiwalled Carbon Nanotube/Polyethersulfone Nanocomposite. *J. Membr. Sci.* **2011**, *375* (1), 284−294.

(25) Li, S.; Liao, G.; Liu, Z.; Pan, Y.; Wu, Q.; Weng, Y.; Zhang, X.; Yang, Z.; Tsui, O. K. Enhanced Water Flux in Vertically Aligned Carbon Nanotube Arrays and Polyethersulfone Composite Membranes. *J. Mater. Chem. A* **2014**, *2* (31), 12171−12176.

(26) Vatanpour, V.; Madaeni, S. S.; Moradian, R.; Zinadini, S.; Astinchap, B. Novel Antibifouling Nanofiltration Polyethersulfone Membrane Fabricated from Embedding TiO₂ Coated Multiwalled Carbon Nanotubes. *Sep. Purif. Technol.* **2012**, *90*, 69−82.

(27) Nie, C.; Ma, L.; Xia, Y.; He, C.; Deng, J.; Wang, L.; Cheng, C.; Sun, S.; Zhao, C. Novel Heparin-mimicking Polymer Brush Grafted Carbon Nanotube/PES Composite Membranes for Safe and Efficient Blood Purification. *J. Membr. Sci.* **2015**, *475*, 455−468.

(28) Vatanpour, V.; Esmaeili, M.; Farahani, M. H. D. A. Fouling Reduction and Retention Increment of Polyethersulfone Nano-filtration Membranes Embedded by Amine-functionalized Multi-walled Carbon Nanotubes. *J. Membr. Sci.* **2014**, *466*, 70−81.

(29) Majeed, S.; Fierro, D.; Buhr, K.; Wind, J.; Du, B.; Boschetti-de-Fierro, A.; Abetz, V. Multi-walled Carbon Nanotubes (MWCNTs) Mixed Polyacrylonitrile (PAN) Ultrafiltration Membranes. *J. Membr. Sci.* **2012**, *403-404*, 101−109.

(30) Xu, H. P.; Lang, W. Z.; Yan, X.; Zhang, X.; Guo, Y. J. Preparation and Characterizations of Poly (vinylidene fluoride)/Oxidized Multi-wall Carbon Nanotube Membranes with Bi-continuous Structure by Thermally Induced Phase Separation Method. *J. Membr. Sci.* **2014**, *467*, 142−152.

(31) Bano, S.; Mahmood, A.; Kim, S. J.; Lee, K. H. Graphene Oxide Modified Polyamide Nanofiltration Membrane with Improved Flux and Antifouling Properties. *J. Mater. Chem. A* **2015**, *3* (5), 2065−2071.

(32) Lee, J.; Chae, H. R.; Won, Y. J.; Lee, K.; Lee, C. H.; Lee, H. H.; Kim, I. C.; Lee, J. M. Graphene Oxide Nanoplatelets Composite Membrane with Hydrophilic and Antifouling Properties for Waste-water Treatment. *J. Membr. Sci.* **2013**, *448*, 223−230.

(33) Yang, L.; Tang, B.; Wu, P. UF Membrane with Highly Improved Flux by Hydrophilic Network Between Graphene Oxide and Brominated Poly (2, 6-dimethyl-1, 4-phenylene oxide). *J. Mater. Chem. A* **2014**, *2* (43), 18562−18573.

(34) Chang, X.; Wang, Z.; Quan, S.; Xu, Y.; Jiang, Z.; Shao, L. Exploring the Synergetic Effects of Graphene Oxide (GO) and Polyvinylpyrrodione (PVP) on Poly (vinylylidenefluoride) (PVDF) Ultrafiltration Membrane Performance. *Appl. Surf. Sci.* **2014**, *316*, 537−548.

(35) Zinadini, S.; Zinatizadeh, A. A.; Rahimi, M.; Vatanpour, V.; Zangeneh, H. Preparation of a Novel Antifouling Mixed Matrix PES Membrane by Embedding Graphene Ooxide Nanoplates. *J. Membr. Sci.* **2014**, *453*, 292−301.

(36) Zhao, Y.; Xu, Z.; Shan, M.; Min, C.; Zhou, B.; Li, Y.; Li, B.; Liu, L.; Qian, X. Effect of Graphite Oxide and Multi-walled Carbon Nanotubes on the Microstructure and Performance of PVDF Membranes. *Sep. Purif. Technol.* **2013**, *103*, 78−83.

(37) Zhang, J.; Xu, Z.; Mai, W.; Min, C.; Zhou, B.; Shan, M.; Li, Y.; Yang, C.; Wang, Z.; Qian, X. Improved Hydrophilicity, Permeability, Antifouling and Mechanical Performance of PVDF Composite Ultrafiltration Membranes Tailored by Oxidized Low-dimensional Carbon Nanomaterials. *J. Mater. Chem. A* **2013**, *1* (9), 3101−3111.

(38) Xu, Z.; Zhang, J.; Shan, M.; Li, Y.; Li, B.; Niu, J.; Zhou, B.; Qian, X. Organosilane-functionalized Graphene Oxide for Enhanced Antifouling and Mechanical Properties of Polyvinylidene Fluoride Ultrafiltration Membranes. *J. Membr. Sci.* **2014**, *458*, 1−13.

(39) Liu, H.; Zhang, G.; Zhao, C.; Liu, J.; Yang, F. Hydraulic Power and Electric Field Combined Antifouling Effect of Novel Conductive Poly(aminoanthraquinone)/Reduced Graphene Oxide Nanohybrid Blended PVDF Ultrafiltration Membrane. *J. Mater. Chem. A* **2015**, *3* (40), 20277−20287.

(40) Wang, Z.; Yu, H.; Xia, J.; Zhang, F.; Li, F.; Xia, Y.; Li, Y. Novel GO−blended PVDF Ultrafiltration Membranes. *Desalination* **2012**, *299*, 50−54.

(41) Zhao, C.; Xu, X.; Chen, J.; Yang, F. Effect of Graphene Oxide Concentration on the Morphologies and Antifouling Properties of PVDF Ultrafiltration Membranes. *J. Environ. Chem. Eng.* **2013**, *1* (3), 349−354.

(42) Yu, L.; Zhang, Y.; Zhang, B.; Liu, J.; Zhang, H.; Song, C. Preparation and Characterization of HPEI-GO/PES Ultrafiltration Membrane with Antifouling and Antibacterial Properties. *J. Membr. Sci.* **2013**, *447*, 452−462.

(43) Zhao, H.; Wu, L.; Zhou, Z.; Zhang, L.; Chen, H. Improving the Antifouling Property of Polysulfone Ultrafiltration Membrane by Incorporation of Isocyanate-treated Graphene Oxide. *Phys. Chem. Chem. Phys.* **2013**, *15* (23), 9084−9092.

(44) Wu, H.; Tang, B.; Wu, P. Development of Novel SiO₂-GO Nanohybrid/Polysulfone Membrane with Enhanced Performance. *J. Membr. Sci.* **2014**, *451*, 94−102.

(45) Safarpour, M.; Khataee, A.; Vatanpour, V. Effect of Reduced Graphene Oxide/TiO₂ Nanocomposite with Different Molar Ratios on the Performance of PVDF Ultrafiltration Membranes. *Sep. Purif. Technol.* **2015**, *140*, 32−42.

(46) Meng, N.; Wang, Z.; Low, Z. X.; Zhang, Y.; Wang, H.; Zhang, X. Impact of Trace Graphene Oxide in Coagulation Bath on Morphology and Performance of Polysulfone Ultrafiltration Membrane. *Sep. Purif. Technol.* **2015**, *147*, 364−371.

(47) Wu, T.; Zhou, B.; Zhu, T.; Shi, J.; Xu, Z.; Hu, C.; Wang, J. Facile and Low-cost Approach Towards A PVDF Ultrafiltration Membrane with Enhanced Hydrophilicity and Antifouling Performance via Graphene Oxide/Water-bath Coagulation. *RSC Adv.* **2015**, *5* (11), 7880−7889.

(48) Wang, J.; Li, Y.; Sun, X. Challenges and Opportunities of Nanostructured Materials for Aprotic Rechargeable Lithium-Air Batteries. *Nano Energy* **2013**, *2* (4), 443−467.

(49) Prince, J.; Bhuvana, S.; Anbharasi, V.; Ayyanar, N.; Boodhoo, K.; Singh, G. Ultra-wetting Graphene-based Membrane. *J. Membr. Sci.* **2016**, *500*, 76−85.

(50) Ganesh, B.; Isloor, A. M.; Ismail, A. Enhanced Hydrophilicity and Salt Rejection Study of Graphene Oxide-Polysulfone Mixed Matrix Membrane. *Desalination* **2013**, *313*, 199−207.

(51) Daraei, P.; Madaeni, S. S.; Ghaemi, N.; Khadivi, M. A.; Astinchap, B.; Moradian, R. Fouling Resistant Mixed Matrix Polyethersulfone Membranes Blended with Magnetic Nanoparticles: Study of Magnetic Field Induced Casting. *Sep. Purif. Technol.* **2013**, *109*, 111−121.

(52) Yang, X.; Zhang, X.; Ma, Y.; Huang, Y.; Wang, Y.; Chen, Y. Superparamagnetic Graphene Oxide-Fe₃O₄ Nanoparticles Hybrid for Controlled Targeted Drug Carriers. *J. Mater. Chem.* **2009**, *19* (18), 2710−2714.

(53) Wang, Z. X.; Lau, C. H.; Zhang, N. Q.; Bai, Y. P.; Shao, L. Mussel-inspired Tailoring of Membrane Wettability for Harsh Water Treatment. *J. Mater. Chem. A* **2015**, *3* (6), 2650−2657.

(54) Li, X.; Fang, X.; Pang, R.; Li, J.; Sun, X.; Shen, J.; Han, W.; Wang, L. Self-assembly of TiO₂ Nanoparticles Around the Pores of PES Ultrafiltration Membrane for Mitigating Organic Fouling. *J. Membr. Sci.* **2014**, *467*, 226−235.

(55) Zhao, W.; Su, Y.; Li, C.; Shi, Q.; Ning, X.; Jiang, Z. Fabrication of Antifouling Polyethersulfone Ultrafiltration Membranes Using Pluronic F127 as Both Surface Modifier and Pore-forming Agent. *J. Membr. Sci.* **2008**, *318* (1), 405−412.

(56) Wang, G.; Chen, G.; Wei, Z.; Dong, X.; Qi, M. Multifunctional Fe₃O₄/Graphene Oxide Nanocomposites for Magnetic Resonance Imaging and Drug Delivery. *Mater. Chem. Phys.* **2013**, *141* (2), 997−1004.

(57) Yu, H.; Li, Y.; Li, X.; Fan, L.; Yang, S. Highly Dispersible and Charge-tunable Magnetic Fe₃O₄ Nanoparticles: Facile Fabrication and Reversible Binding to GO for Efficient Removal of Dye Pollutants. *J. Mater. Chem. A* **2014**, *2* (38), 15763−15767.

(58) Bai, L. Z.; Zhao, D. L.; Xu, Y.; Zhang, J. M.; Gao, Y. L.; Zhao, L. Y.; Tang, J. T. Inductive Heating Property of Graphene Oxide-Fe₃O₄ Nanoparticles Hybrid in An AC Magnetic Field for Localized Hyperthermia. *Mater. Lett.* **2012**, *68*, 399−401.

(59) Chandra, V.; Park, J.; Chun, Y.; Lee, J. W.; Hwang, I. C.; Kim, K. S. Water-dispersible Magnetite-reduced Graphene Oxide Composites for Arsenic Removal. *ACS Nano* **2010**, *4* (7), 3979−3986.

(60) Qin, A.; Li, X.; Zhao, X.; Liu, D.; He, C. Engineering A Highly Hydrophilic PVDF Membrane via Binding TiO_2 Nanoparticles and a PVA Layer onto a Membrane Surface. *ACS Appl. Mater. Interfaces* **2015**, *7* (16), 8427−8436.

(61) Hong, J.; He, Y. Polyvinylidene Fluoride Ultrafiltration Membrane Blended with Nano-ZnO Particle for Photo-catalysis Self-cleaning. *Desalination* **2014**, *332* (1), 67−75.

(62) Rana, D.; Matsuura, T. Surface Modifications for Antifouling Membranes. *Chem. Rev.* **2010**, *110* (4), 2448−2471.

(63) Yan, L.; Li, Y. S.; Xiang, C. B.; Xianda, S. Effect of Nano-sized Al_2O_3-Particle Addition on PVDF Ultrafiltration Mmembrane Pperformance. *J. Membr. Sci.* **2006**, *276* (1), 162−167.

(64) Xia, S.; Ni, M. Preparation of Poly (vinylidene fluoride) Membranes with Graphene Oxide Addition for Natural Organic Matter Removal. *J. Membr. Sci.* **2015**, *473*, 54−62.

(65) Damodar, R. A.; You, S. J.; Chou, H. H. Study the Self Cleaning, Antibacterial and Photocatalytic Properties of TiO_2 Entrapped PVDF Membranes. *J. Hazard. Mater.* **2009**, *172* (2), 1321−1328.

(66) Liang, S.; Qi, G.; Xiao, K.; Sun, J.; Giannelis, E. P.; Huang, X.; Elimelech, M. Organic Fouling Behavior of Superhydrophilic Polyvinylidene Fluoride (PVDF) Ultrafiltration Membranes Functionalized with Surface-tailored Nanoparticles: Implications for Organic Fouling in Membrane Bioreactors. *J. Membr. Sci.* **2014**, *463*, 94−101.

(67) Liu, Y.; Su, Y.; Zhao, X.; Li, Y.; Zhang, R.; Jiang, Z. Improved Antifouling Properties of Polyethersulfone Membrane by Blending the Amphiphilic Surface Modifier with Crosslinked Hydrophobic Segments. *J. Membr. Sci.* **2015**, *486*, 195−206.

(68) Liu, Y.; Xu, L.; Song, Y.; Fu, X.; Zou, J.; Hu, X.; Jiang, Z.; Zhao, X. Investigation of Antifouling Universality of Polyvinyl Formal (PVF) Membranes Utilizing Atomic Force Microscope (AFM) Force Curves. *RSC Adv.* **2015**, *5* (46), 36894−36901.

(69) Miao, R.; Wang, L.; Wang, X.; Lv, Y.; Gao, Z.; Mi, N.; Liu, T. Preparation of A Polyvinylidene Fluoride Membrane Material Probe and Its Application in Membrane Fouling Research. *Desalination* **2015**, *357*, 171−177.

(70) Hashino, M.; Hirami, K.; Ishigami, T.; Ohmukai, Y.; Maruyama, T.; Kubota, N.; Matsuyama, H. Effect of Kinds of Membrane Materials on Membrane Fouling with BSA. *J. Membr. Sci.* **2011**, *384* (1), 157−165.